Thermoelectric properties and low thermal conductivity of nanocomposite $ZrTe_5$ under magnetic field

Aymeric Ramiere[1]*, Fu Li[1], Yuexing Chen[1], and Yongqing Fu[2]

[1]Shenzhen Key Laboratory of Advanced Thin Films and Applications, College of Physics and Optoelectronic Engineering, Shenzhen University 518060, China

[2]Faculty of Engineering and Environment, Northumbria University, Newcastle upon Tyne, NE1 8ST, United Kingdom

*Corresponding author: ramiere@szu.edu.cn

ABSTRACT:

Zirconium pentatelluride ($ZrTe_5$) single crystal has recently received significant attention because of its quantum electronic transport properties and is regarded as a promising candidate for low-temperature thermoelectric cooling and spintronic applications. However, single crystal of $ZrTe_5$ has generally small sizes and can only be produced in small quantities using a complicated process, whereas $ZrTe_5$ polycrystals are easily produced and their properties are easily adjusted. In this study, we focus on the magneto-transport properties at low temperatures of nanocomposites of $ZrTe_5$ produced using both hand-milling and ball-milling processes to investigate the impact of microstructure. The ball-milled sample shows a low thermal conductivity of 1 $W.m^{-1}.K^{-1}$, which is almost a constant below 300 K. However, due to its small grain sizes, the electron mobility is significantly decreased, thus their thermoelectric performances are not as good as that of the hand-milled sample. Also, below 25 K, the resistivity and the Seebeck coefficient of the ball-milled sample are decreased, which is associated with the energy barrier at their grain boundaries. Due to the larger grain sizes and fewer defects in the hand-milled sample, the external magnetic field shows a significant influence on its thermoelectric properties at low temperatures. These results indicate that polycrystalline $ZrTe_5$ with large grain sizes may exhibit similar quantum properties as those of single crystals.

KEYWORDS:

$ZrTe_5$ nanocomposite; thermoelectric properties; microstructure; high-energy ball milling; grain boundaries; magnetic measurements

1. INTRODUCTION

Thermoelectric coolers (TECs) use the Peltier effect to create a temperature gradient when an electric current is applied through the material [1], whereas thermoelectric generators (TEGs) are based on the reverse of the Seebeck effect. Although the TEGs work at relatively high temperatures to convert the heat gradient into electricity, they also work at low temperatures as effective refrigeration devices [2]. Their performance can be estimated by the figure of merit: $ZT = S^2T/(\rho\kappa)$, where S is the Seebeck coefficient, ρ the electrical resistivity, κ the thermal conductivity and T the absolute temperature. Over the past twenty years, various types of TECs have been extensively studied because they are reliable, compact, without liquid or vibrations and environment friendly, and have advantages over the traditional cooling systems [3,4]. TECs have many applications, not only in microelectronic devices [5–8], but also in air conditioning [9,10] and wearable cooling system [11].

Single crystal of zirconium pentatelluride ($ZrTe_5$) has long been regarded as a potential candidate for the TECs because its power factor maintains a high value when the temperature decreases [12–14]. For example, Guo *et al*. recently showed that the *ZT* value of $ZrTe_5$ nanoribbons is increased up to five times with a decrease of their thicknesses if compared with those of bulk crystals [15]. Zhang *et al*. also reported that nanostructured $ZrTe_5$ crystals exhibit one order magnitude reduction in the thermal conductivity compared to the conventional crystals [16]. Over the past a few years, $ZrTe_5$ single crystal has received significant attention due to its exceptional topological properties. It is proved to be a two-dimensional topological insulator with a quantum spin Hall effect [17–19] and it displays behaviors of either weak topological insulator or strong topological insulator depending on the interlayer spacing in the crystal structure [20–22]. $ZrTe_5$ has also been reported as a three-dimensional Dirac semimetal with

Zeeman splitting [23–25] effect and exhibits a chiral magnetic effect with a negative magnetoresistance [26]. Very recently, an anomalous Hall effect and a three-dimensional quantum Hall effect were observed in the $ZrTe_5$ with an exotic quantum nature [27,28]. Furthermore, magneto-transport measurements showed that $ZrTe_5$ single crystal is a promising candidate for spintronic device applications [18,20,25].

However, single crystals of $ZrTe_5$ are generally difficult to be synthesized, and the commonly used methods are chemical vapor transport [19,29] or the flux method [28,30]. Only a small quantity of crystals can be made in each process and the sizes of the single crystals are usually quite small. In comparison, polycrystals of $ZrTe_5$ can be produced easily, rapidly, in a large quantity and with controllable sizes. Hooda *et al.* and Miller *et al.* recently explored the thermoelectric properties of polycrystalline $ZrTe_5$, measured at low temperatures [31,32]. Both these studies used similar procedures for the synthesis of the $ZrTe_5$ polycrystals and the thermoelectric measurements. However, these two studies showed quite different results of the electrical resistivity and Seebeck coefficient. Hooda *et al.* observed a very high resistivity above 100 mW.cm. They also found a transition from semiconductor to semimetal at 150 K but the resistivity was increased exponentially as the temperature decreases. The Seebeck coefficient was increased as the temperature was increased, with a short plateau near 38 K (which was attributed to an anomaly in the density of states of $ZrTe_5$), but it exceeded 450 $mV.K^{-1}$ above 300 K [31]. Whereas Miller *et al.* observed a resistivity which was two orders of magnitude lower, around 2 mΩ.cm, and it decreased below 90 K and the Seebeck coefficient peaked at 130 $mV.K^{-1}$ at 150 K and then decreased as the temperature was increased. Miller *et al.* proved that the polycrystalline $ZrTe_5$ is a narrow-bandgap semiconductor based on a two-band model [32]. They also showed the highest thermoelectric performance with ZT~0.15 at 300 K. In another study,

Chen *et al.* synthesized Te-rich $ZrTe_{5+\delta}$ polycrystals, which have a relatively low thermal conductivity but a large electrical resistivity and poor thermoelectric performance (with *ZT* of ~0.04) at 300 K [33]. The discrepancies in the results obtained by different studies show that it is critical to systematically study the thermoelectric properties of polycrystalline $ZrTe_5$.

The high-energy ball-milling method is well-known to enhance the thermoelectric performance of polycrystalline materials and was successfully applied in different materials such as bismuth telluride and silicon germanium with more than 30% increase in *ZT* [34,35]. It creates nanocomposites with a microstructure composed of a variety of crystallite sizes ranging from nanometers to micrometers which effectively scatters phonons and achieves a very low thermal conductivity. We believe that the nanocomposites of $ZrTe_5$ obtained using a ball-milling process may exhibit better thermoelectric performance than those obtained by hand-milling reported in the literature[31–33].

In this paper, we prepare two types of $ZrTe_5$ nanocomposites using both ball-milling and hand-milling processes to study the effects of microstructures on the thermoelectric properties and understand the physical properties of polycrystalline $ZrTe_5$. It is currently unknown if the topological quantum properties still persist in polycrystalline $ZrTe_5$ at very low temperatures, which is important for further applications. Therefore, we characterized thermoelectric properties of nanocomposite $ZrTe_5$ as a function of temperature below 380 K and also with an external magnetic field up to 12 T at 25 K. Our results show that $ZrTe_5$ nanocomposite with a large grain size yields a better *ZT* value and responds better to the external magnetic field.

2. EXPERIMENTAL DETAILS

Following the standard preparation procedures of $ZrTe_5$ powders reported in the literature [36], we mixed pure elements of Zr and Te in stoichiometric proportions in a quartz tube, which was pre-evacuated at a pressure below 2×10^{-4} Pa. Then the tubes were slowly heated to 480 ˚C, held at this temperature for ten days and finally slowly cooled down to room temperature. Two types of polycrystalline $ZrTe_5$ composites were made: one with relatively large grains and the other with small grains. To make large grains of polycrystals, the obtained compound was hand-milled in an agate mortar for twenty minutes and then sintered using a spark plasma sintering (SPS) method at 400 ˚C with a pressure of 40 atm for 10 min. The small grain sample was obtained by high-energy planetary ball milling under a vacuum of 8×10^{-3} Pa with a ball rotation speed of 450 rpm for 4 hours. Then the ball-milled powders were SPS sintered at a temperature of 350 ˚C. The SPS process was selected in this study because it allows a better control of the nanostructures by preventing grain size growth due to its fast heating and cooling rates in a high vacuum[37].

Before sintering, the powders were characterized by X-ray diffraction (XRD) using a Rigaku Ultima IV diffractometer with a discrete step of 0.01˚ from 10˚ to 90˚ to quantitatively analyze the crystallinity of the samples. After sintering, the microstructure of the samples was characterized using a scanning electron microscope (SEM, Thermo Scientific™ Scios™). The chemical composition of the sample was determined using an energy-dispersive X-ray spectroscope (EDS, Ametek EDAX). EDS spectra were acquired with a beam energy of 30 keV and a duration of 1000 s each.

The thermoelectric properties of the samples were measured using a physical property measurement system (PPMS, Quantum Design, Inc.) with the thermal transport option (TTO). A

square rod of 2×2×12 mm^3 was cut from the pellet and the facets were mirror polished. Copper wires were attached to the rod with conductive silver paste for four-probes measurements. A copper shield was put around the sample and a high vacuum of below 8.10^{-6} Pa were used to minimize the thermal losses by radiation and convection, respectively. The temperature of the sample was controlled from 380 K down to ~10 K. At 25 K, the magnetic field was scanned from -12 T to 12 T. Thermoelectric properties of the samples were acquired when the temperature difference between the hot and cold sides is 5% and when both hot and cold temperatures became stable within 1% error. These temperature stability settings were chosen in this study to obtain reliable and high-quality data, although they became increasingly difficult to control in some cases thus limiting our measurements as it will be shown later.

3. RESULTS AND DISCUSSION

3.1 Microstructures and physical properties

XRD patterns of the powders obtained by hand-milling and ball-milling are shown in Fig. 1. Both the samples contain one single-phase corresponding to the space group *Cmcm* that is characteristic of the orthorhombic layered structure of $ZrTe_5$ (ICSD #085506) [38]. The two samples show different peak intensities and their $ZrTe_5$ microcrystals have different orientations. The reason is that $ZrTe_5$ has a layered structure along the b-axis and tends to grow in a ribbon shape. The large crystals in the hand-milled sample tend to be self-aligned in the in-plane direction when the powders are packed for measurement with the b-axis facing up, e.g., with the large intensities of the (020) and (041) peaks. The smaller microcrystals for the ball-milled sample have a relatively isotropic distribution, and their XRD pattern is noisier and shows much

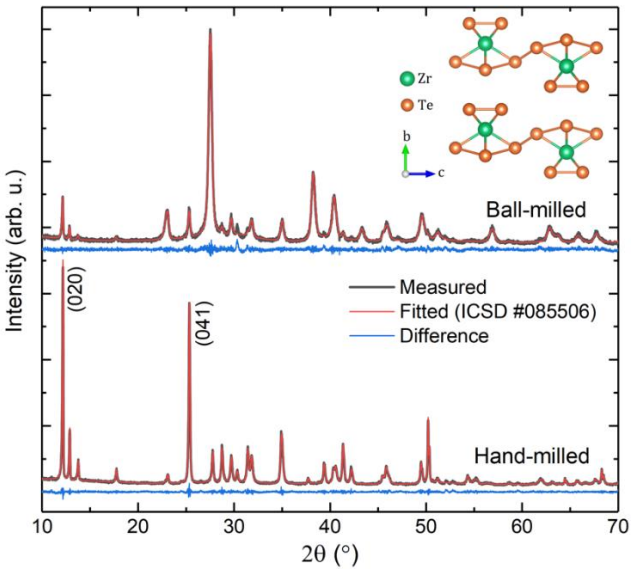

Fig. 1: X-ray diffraction measurements of hand-milled and ball-milled samples. The inset shows the crystal structure of $ZrTe_5$.

broader peaks due to lattice defects and nanocrystallite sizes caused by the high-energy milling process.

The crystallinity of the samples was determined using a Rietveld refinement analysis (further details in Supplementary Material). Results indicate both the powders have similar unit cells with $a = 3.98$ Å, $b = 14.52$ Å and $c = 13.72$ Å which are in very good agreements with published results in literature [39]. The average crystallite size and lattice strain were estimated using the Halder-Wagner method [40]. We found that the hand-milled sample has an average crystallites size of ~600 nm and a strain of 0.2% while the ball-milled sample has an average crystallites size of 240 nm and a strain of 0.5%. Although these values are estimations that are limited by the Halder-Wagner method [41,42], the similar treatment of the data allows for a comparison between the samples. We notice that the ball-milled sample has half of the crystallites size but

twice as much strain than those of the hand-milled sample. The higher level of strain indicates that the ball-milled sample contains significantly more defects than the hand-milled sample.

A piece of each sintered sample was cleaved along both the parallel and perpendicular directions to observe the microstructure using the SEM. Figs. 2(a) to 2(d) show that both the hand-milled and the ball-milled samples have similar morphology with microcrystals homogeneously distributed inside a matrix of nanocrystals. Therefore, they both can be categorized as nanocomposites. The hand-milled nanocomposite is mainly composed of microcrystals of tens of micrometers with a layered structure and the nanocrystals are around a hundred nanometers. The ball-milled nanocomposite has only a few microcrystals that are still maintained after the high-energy milling process and most of the sample is composed of nanocrystals with sizes of a few tens of nanometers. These observations are in good agreement with those from the XRD data.

Fig. 2(e) shows the EDS spectra of the samples, for both the microcrystals and the matrix of nanocrystals. The EDS spectra of the microcrystals for both the hand-milled (spot 1) and ball-milled (spot 3) samples are similar, with an atomic ratio of Zr:Te≈1:4.99, very close to the ideal ratio. The spectra acquired at the nanocrystal sites for both the samples show a reduction of the peaks around 0.5 keV, corresponding to the outer M shell of Te. The atomic ratio in these nanocrystals in the hand-milled sample is Zr:Te≈1:4.94 (spot 2). The Te M peak is almost disappeared in the nanocrystals of the ball-milled sample and the atomic ratio is Zr:Te≈1:4.90 (spot 4). The overall chemical composition was acquired on a 200×200 μm^2 and show an average atomic ratio of Zr:Te≈1:4.97 for the hand-milled sample and only 1:4.91 for the ball-milled sample. The Te deficiency in the ball-milled sample is supposed to originate from a weak bonding of the Te M shell. We assume that these bonds have been damaged during the milling

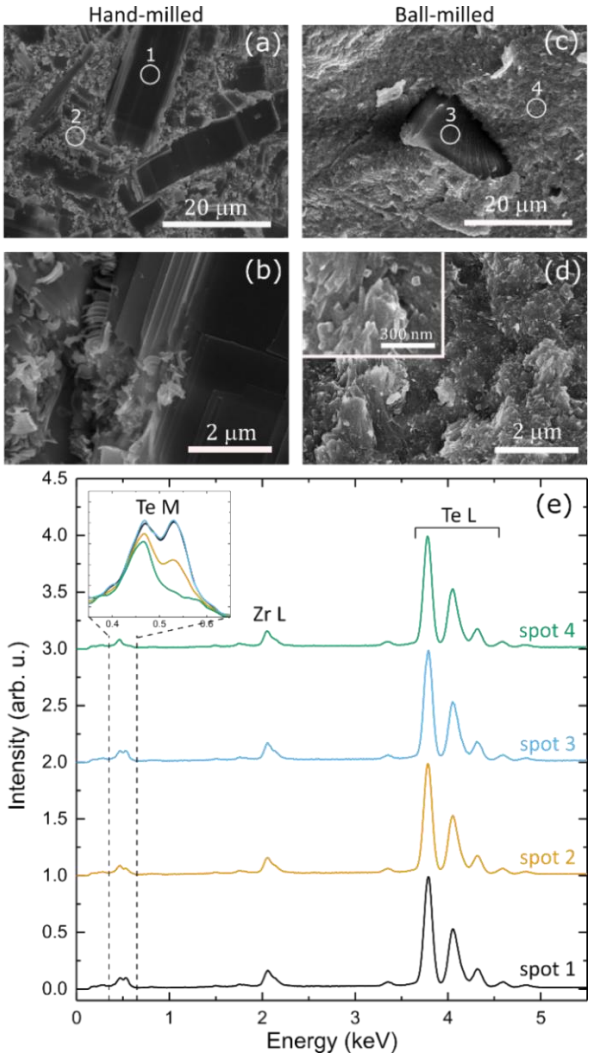

Fig. 2: SEM images of $ZrTe_5$ nanocomposites. (a) and (b) show the hand-milled sample. (c) and (d) show the high-energy ball-milled sample. (e) EDS spectra at different locations indicated in the SEM images.

process and more defects are introduced with higher energy milling, and the large strain measured by XRD is certainly related to the Te deficiency in this crystal structure.

The density of the samples was measured using the Archimedes' buoyancy technique. The density of the hand-milled sample is 5.78 g/cm^3 which is lower than 6.03 g/cm^3 measured for the ball-milled sample. As expected, the ball-milled sample is denser due to the smaller crystals that

are more tightly packed together. Both the densities are close to the theoretical density of 6.09 g/cm^3 of the single crystal so that porosity effects can be neglected.

3.2 *zT* values vs temperature

Fig. 3 summarizes the thermoelectric properties as a function of temperature. We compare the hand-milled sample measurements to the results by Miller *et al.* [32]. and Hooda *et al.* [31]. Figs. 3(a), 3(b) and 3(d) clearly show that our results are in good agreements with those of Miller *et al.*, suggesting that there is a similar microstructure between the samples with similar physical properties where nanocomposite $ZrTe_5$ can be modeled as a narrow-bandgap semiconductor [32].

However, our results are quite different from those of Hooda *et al.* [31]. This is quite puzzling because their preparation of the powder and characterization method are similar to ours and those from Miller *et al.* [32]. From the Zr-Te phase diagram [43], one possible explanation may be that there is a partial phase transition from $ZrTe_5$ to $ZrTe_3$ that happens around 450 ˚C. This is because, during the sintering process, Hooda *et al.* used a long time (24 hours) hot pressing at 500 ˚C. This observation highlights the importance of the careful preparation of polycrystalline $ZrTe_5$. We suggest using a sintering temperature below 450 ˚C to avoid such a possible phase transition.

Comparing the results obtained from our two samples, we observe that the thermoelectric properties of the ball-milled sample and the hand-milled sample are quite different. Transport properties in the hand-milled sample are dominated by the intrinsic features of the $ZrTe_5$ crystals because the obtained results can be explained by assuming that the nanocomposite is a narrow-bandgap semiconductor. However, the transport properties in the ball-milled sample are strongly

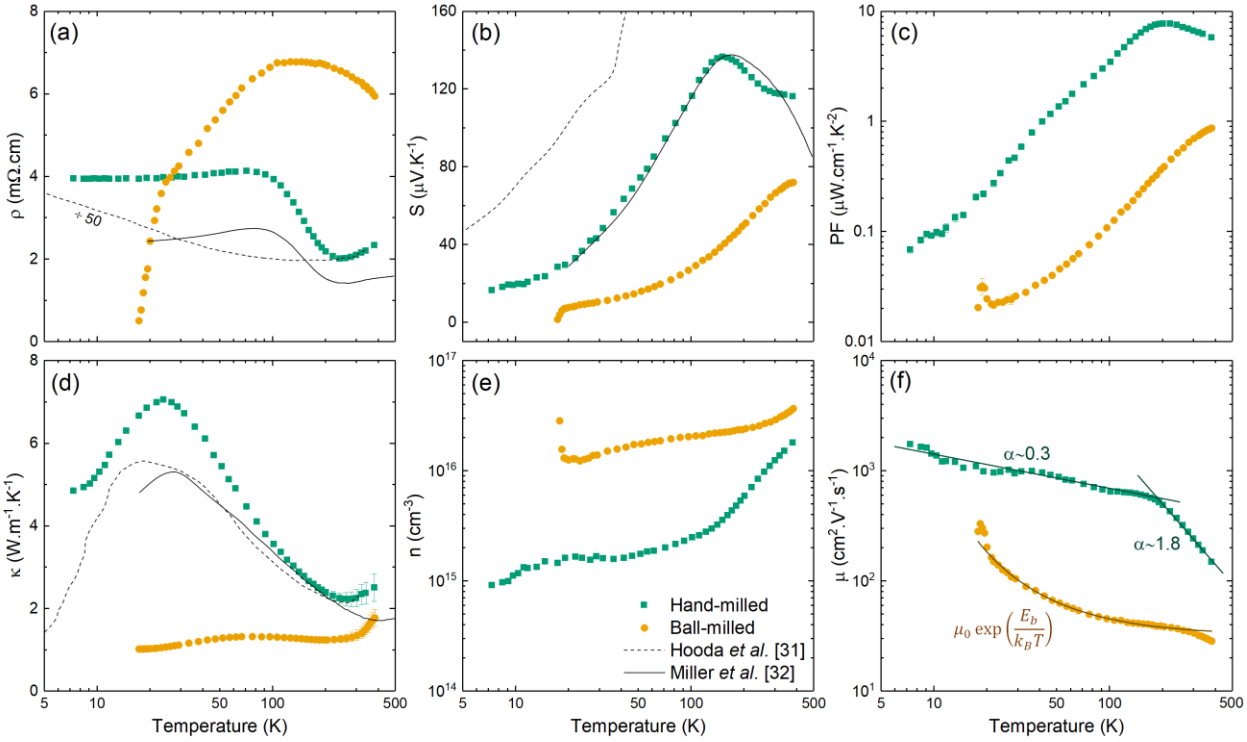

Fig. 3: Thermoelectric properties measurements of hand-milled and ball-milled samples as a function of temperature and comparison with literature data [31, 32] for (a) resistivity, (b) Seebeck coefficient, (c) power factor, (d) thermal conductivity, (e) carrier concentration, and (f) mobility. Fitting curves in (f) correspond to different scattering mechanisms.

influenced by the microstructure. The ball-milled sample shows intriguing electrical features at very-low temperature as the resistivity decreases rapidly below 25 K which is closely followed by a decrease of the Seebeck coefficient below 20 K. Both these two trends result in a small peak of the power factor $PF = S^2/\rho$ around 20 K, as shown in Fig. 3(c). Further analysis shows that this change is related to the microstructure of the ball-milled sample. The Seebeck coefficient becomes close to zero at 17 K, which was the lowest temperature we could achieve with this sample. Following the trend, the Seebeck coefficient would change sign at around 15 K to transition from p-type to n-type dominant carrier. Theoretical calculations from literature

predicted that this kind of transition occurs in n-type doped $ZrTe_5$ with a doping concentration below 10^{19} cm^3 and the transition temperature occurs at a lower temperature when the doping concentration is decreased [32,39]. We correlate this n-type doping to the Te deficiency that has induced additional electrons in the ball-milled sample. Ref. [32] reported that the lowest calculated doping concentration is 10^{16} cm^3 which shows a temperature transition around 35 K. Fig. 3(e) shows that the total carrier concentration in the ball-milled sample is also around 10^{16} cm^3, thus it is expected that the doping concentration could be lower, hence a lower transition temperature was obtained.

Even though the base temperature of the PPMS refrigerator is 2 K, the sample temperature could only be lowered down to 7 K due to the thermal load caused by the size of the sample. Besides, despite two attempts, the temperature of the ball-milled samples could not be stabilized below 17 K, therefore, we did not acquire any measurements below this temperature.

The bandgap can be estimated by using the peak of the Seebeck coefficient [1] based on the equation of $S(T_p) \sim E_g/(2eT_p)$. We obtained the value of $E_g \sim 40\ meV$ for the hand-milled sample which is in agreement with that from the APRES measurements [22]. The ball-milled sample has a wider bandgap with a value of $E_g \sim 55\ meV$. This could be due to the impact of the microstructure on the electronic band structure which is consistent with the lowering energy level of the valence band caused by doping [44].

For metals and degenerated semiconductors (parabolic band and energy independent scattering approximations), the Seebeck coefficient is given by [45]:

$$\alpha = \frac{8\pi^2 k_B^2}{3eh^2} m^* T \left(\frac{\pi}{3n}\right)^{2/3}, \quad (1)$$

where k_B is the Boltzmann constant, h is the Planck constant, m^* is the carriers' effective mass and n is the carrier concentration. We set $m^* = 0.15m_e$, with m_e the mass of the electron, according to previous studies [24,32] and use Eq. 1 to determine the effective carrier concentration as a function of temperature, and the results are shown in Fig. 3(e). Then the carrier mobility μ can be obtained by using the resistivity measurements, based on the following equation:

$$\sigma = 1/\rho = n\, e\, \mu, \tag{2}$$

where e is the electron charge. The results of mobility are shown in Fig. 3(f). The temperature-dependent mobility indicates that the transport properties of the samples are dominated by scattering mechanisms. The hand-milled sample shows two different linear regions in the log-log plot, with the slope defined by $\alpha = dlog(\mu)/dlog(T)$. Above 190 K, $\alpha \sim -1.8$. This value is relatively close to $-3/2$ which is the characteristic of a dominant acoustic phonon scattering [46]. Below 190 K, the slope becomes smaller with $\alpha \sim 0.3$ because of the interplay of other scattering mechanisms, for example, the ionized impurities. The mobility of the ball-milled sample can be explained by the scattering at the grain boundaries of the nanocrystals, which can be described by [47]:

$$\mu_b(T) = \mu_0 \exp\left(\frac{E_b}{k_B T}\right), \tag{3}$$

where μ_0 is the effective mobility and E_b the inter-grain energy barrier. By fitting our data of the ball-milled sample, we find $\mu_0 = 32\ cm^2.V^{-1}.s^{-1}$ and $E_b = 3\ meV$. This inter-grain energy barrier corresponds to a thermal energy of 23 K. Therefore, we can link the change in behavior of the resistivity and Seebeck coefficient in the ball-milled sample below 25 K with the modified electron transmission and the overcome of the energy barrier at the grain boundaries.

The thermal conductivity of the hand-milled samples peaks at 24 K with $\kappa = 7\ W.m^{-1}.K^{-1}$. This high thermal conductivity is caused by the large grains in the hand-milled sample that allow phonons to have long mean free paths [48]. Above 300 K, the thermal conductivity is increasing which is due to the bipolar diffusion. In this case, both electrons and holes contribute to the thermal conductivity, which is coherent with the narrow-bandgap nature of the hand-milled sample. As expected, the ball-milled sample has a much lower thermal conductivity because of the abundant interfaces created by the nanocrystals and defects induced by the Te deficiency that scatters phonons efficiently [34,49]. The thermal conductivity is close to 1 $W.m^{-1}.K^{-1}$ throughout the whole temperature range, close to the lower limit value of 0.73 $W.m^{-1}.K^{-1}$ estimated theoretically [50].

The thermal conductivity values at the low temperatures can be used to determine the average phonon mean free path as a function of temperature, which can be linked with the microstructure of the samples. The Wiedemann-Franz law [31] is used to obtain the lattice thermal conductivity due to phonons, $\kappa_{ph} = \kappa - LT/\rho$, where $L = 2.4 \times 10^{-8} J^2.C^{-2}.K^{-2}$ is the Lorentz number. We use this formula only when it is below 250 K where the bipolar effect can be neglected. The phonon mean free path Λ_{ph} can be calculated using the kinetic theory [46]:

$$\kappa_{ph} = \frac{1}{3} C_V v \Lambda_{ph} \tag{4}$$

where C_V is the heat capacity as measured by Shaviv *et al.* [51] (see supplementary material) and $v = 1632 m.s^{-1}$ the average sound velocity calculated by the density functional theory (DFT) [50]. At the lowest temperature, Λ_{ph} in the hand-milled sample reaches several hundred nanometers, close to the estimated crystallite size determined by XRD. This shows that the heat transport is limited by phonon scattering at the grain boundaries. However, the value of Λ_{ph} in the ball-milled sample is smaller

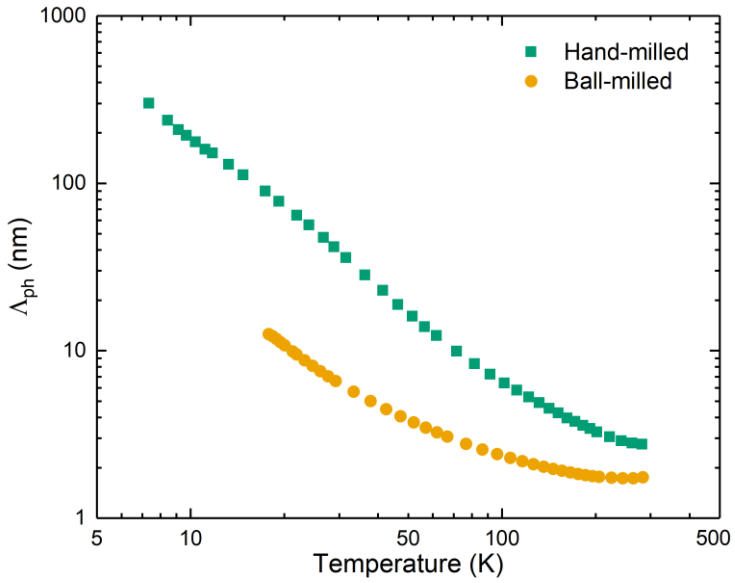

Fig. 4: Phonon mean free path Λ_{ph} below 250 K calculated with Eq. 4.

than the estimated crystallites size (with only tens of nanometers), suggesting that a fraction of the phonons is scattered by the defects created by the Te vacancies.

The thermoelectric figure of merit shows a peak around 340 K with *ZT*=0.09 in the hand-milled sample while the *ZT* is only 0.02 for the ball-milled sample. The reduced *ZT* value of the ball-milled sample comes from the strong increase of the power factor that exceeds the reduction of the thermal conductivity. Also, the *ZT* value of the ball-milled sample shows a local maximum at 20 K, caused by the peak of the power factor, as discussed earlier. These results show that there is room for improvement in the thermoelectric properties of $ZrTe_5$ by carefully engineering the microstructure.

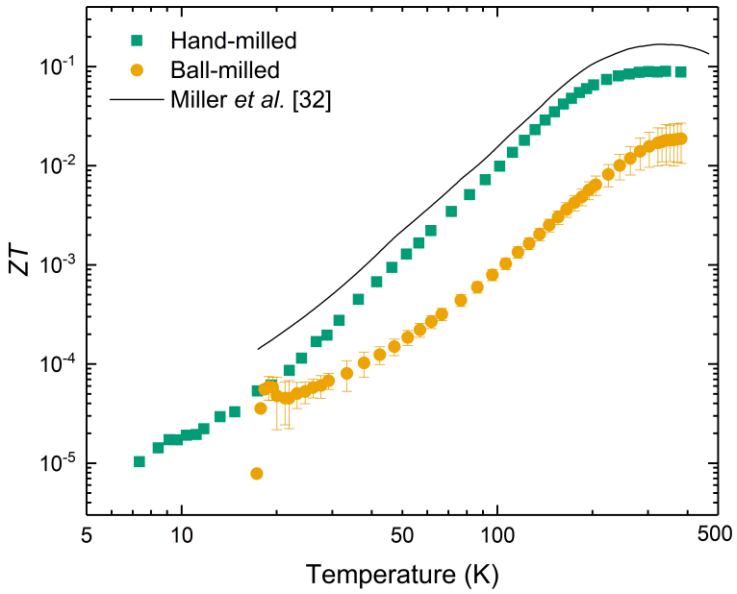

Figure 5: Figure of merit for the hand-milled and ball-milled samples and comparison with ref. [32]

3.3 *ZT* values vs magnetic field

Fig. 6 shows the thermoelectric properties under an external magnetic field B up to ±12 T at a temperature T~25 K which is the lowest temperature where the magnetic field can be scanned without significant errors caused the magnetization of the thermometers on the samples. We observe that the transport properties in the ball-milled sample do not change with the magnetic field, which is attributed to the scattering at the grain boundaries of the nanocrystals. On the other hand, the hand-milling sample has relatively large crystallites so that the magnetic field has a significant impact on the electronic transport.

According to our previous results on single-crystal $ZrTe_5$ [25], the premise of the Shubnikov-de-Haas oscillations due to the quantum Hall effect could be visible at 25 K by a flattening of $\rho(B)$ around 3 T and a decreasing trend above 10 T. Though the flattening may be subtle (we performed a detailed sweep around 3T to try and observe it), the turn-around at 10 T should still

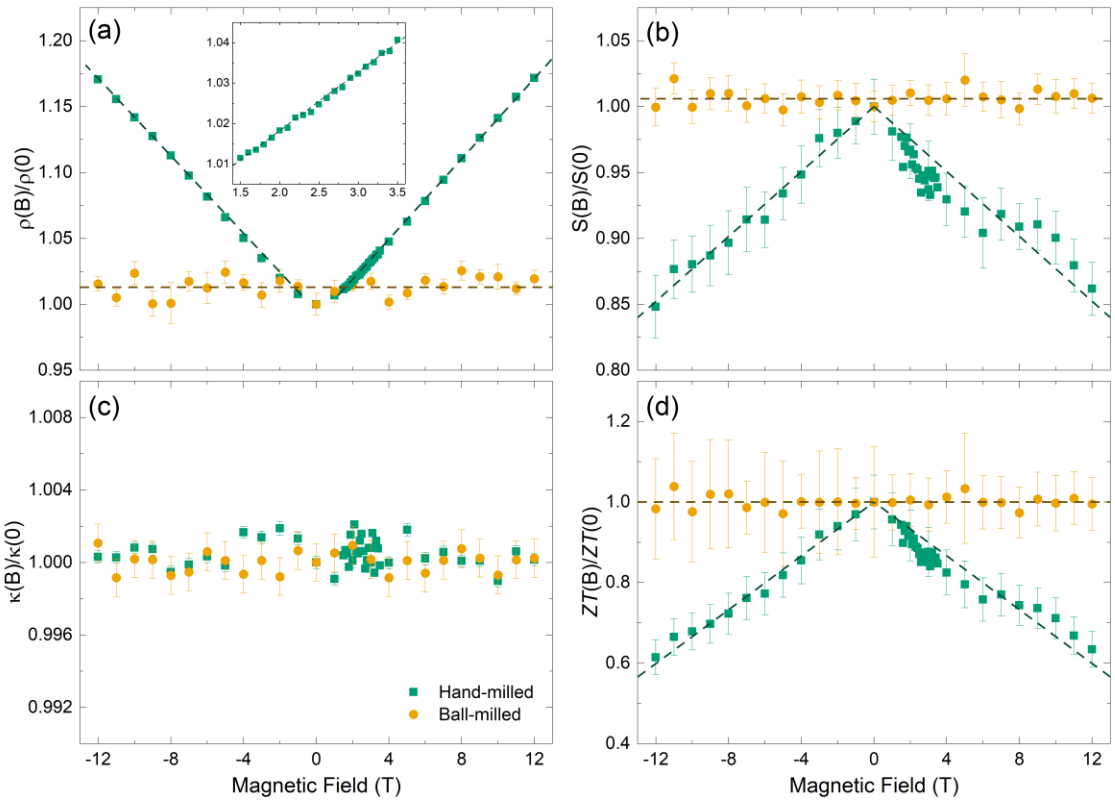

Figure 6: Thermoelectric properties measurements of hand-milled and ball-milled samples as a function of the magnetic field for (a) resistivity, (b) Seebeck coefficient, (c) thermal conductivity and (d) *ZT*. Results are normalized with the value at $B = 0$. Dashed lines are guides for the eyes. The inset in (a) shows the detailed scan of the resistivity in the region 1.5 T to 3.5 T.

be observable. However, Fig. 6(a) shows that the resistivity of the hand-milled sample increases linearly through the entire range of the magnetic field. Besides, we notice that from $B = 0$ to 10 T, the ratio of $\rho(B)/\rho(0)$ increases by 70% for the single crystal but it increases by only 15% in the hand-milled nanocomposite. It means that the scattering rate is much less affected by the magnetic field in the nanocomposite. The absence of quantum effect in the nanocomposite may be due to the existence of defects inherent to the preparation of the polycrystal itself and/or the

interactions of the packed microcrystals that change the nature of the electron scattering compared to the single crystal.

Fig. 6(b) shows that the Seebeck coefficient decreases linearly with the magnetic field for the hand-milled sample. This decrease is related to the increase of the magnetoresistance which originates from the increase of the electron scattering with the magnetic field. For example, when the magnetic field is increased from 0 to 10 T, the Seebeck coefficient decreases by 12% which is relatively close to the variation of the resistivity. Both the resistivity and the Seebeck coefficient are symmetrical regarding $B = 0$, showing the isotropic distribution of the orientation of the microcrystals in the hand-milled sample. We observe from Fig. 6(c) that the thermal conductivity does not change with the magnetic field. This was expected because the thermal transport at very low temperature is almost entirely due to phonons that are unaffected by the magnetic field. Regarding the resistivity and Seebeck coefficient, the resulting zT of the hand-milled sample, shown in Fig. 6(d), displays a logical linear decrease with the magnetic field.

There is a clear trend of the increase of the resistivity with the magnetic field for the hand-milled sample as shown in Fig. 6(a). It indicates that polycrystalline $ZrTe_5$ maintains significant spin interactions from its single crystal form. Optimization of the synthesis process to achieve larger crystal sizes and fewer nanocrystals should yield a higher magnetoresistance ratio that could be more promising for spintronic applications.

4. CONCLUSIONS

Our studies showed that the microstructure has a strong impact on the thermoelectric properties of nanocomposite $ZrTe_5$. Compared to those of the hand-milling process, we have

shown that the ball-milling process had two influences on the microstructure: (1) it strongly reduced the grain sizes to create a homogenous matrix of nanocrystallites; and (2) it induced a Te deficiency. The nanocrystallites caused a strong scattering of both the phonons and the electrons at the grain boundaries which dominated the transport properties in the ball-milled sample. Therefore, the ball-milled sample had a low thermal conductivity and a low electron mobility. The Te deficiency increased the carrier concentration but its impact was not as significant as that of the grain boundary scattering, thus leading to a reduction of the power factor by almost one order of magnitude. Overall, the electrical transport properties of the ball-milled sample were deteriorated and could not be compensated by its very low thermal conductivity. Therefore, this leads to a reduction of the thermoelectric performance of the ball-milled sample compared to that of the hand-milled sample. We also observed a decrease in the resistivity and Seebeck coefficient below 25 K that can be related to the overcome of the energy barrier at the grain boundaries. The magneto-transport measurements at 25 K show that a synthesis process creating bigger crystallites should be used to enhance the magnetic field effect on the electronic properties.

ACKNOWLEDGMENTS

This work was supported by the Shenzhen University start-up fund (No. 860-000002110199), and UK Newton Mobility Grant (No. IE161019) through Royal Society and NSFC, as well as Royal Academy of Engineering UK-Research Exchange with China and India.

REFERENCES

[1] H.J. Goldsmid, Introduction to Thermoelectricity, 2nd editio, Springer, 2016. https://doi.org/10.1007/978-3-662-49256-7.

[2] D. Enescu, E.O. Virjoghe, A review on thermoelectric cooling parameters and performance, Renew. Sustain. Energy Rev. 38 (2014) 903–916. https://doi.org/10.1016/j.rser.2014.07.045.

[3] L.E. Bell, Cooling, Heating, Generating Power, and Recovering Waste Heat with Thermoelectric Systems, Science. 321 (2008) 1457–1461. https://doi.org/10.1126/science.1158899.

[4] D. Zhao, G. Tan, A review of thermoelectric cooling: Materials, modeling and applications, Appl. Therm. Eng. 66 (2014) 15–24. https://doi.org/10.1016/j.applthermaleng.2014.01.074.

[5] M. Zebarjadi, Electronic cooling using thermoelectric devices, Appl. Phys. Lett. 106 (2015) 203506. https://doi.org/10.1063/1.4921457.

[6] W. He, G. Zhang, X. Zhang, J. Ji, G. Li, X. Zhao, Recent development and application of thermoelectric generator and cooler, Appl. Energy. 143 (2015) 1–25. https://doi.org/10.1016/j.apenergy.2014.12.075.

[7] G. Bulman, P. Barletta, J. Lewis, N. Baldasaro, M. Manno, A. Bar-Cohen, B. Yang, Superlattice-based thin-film thermoelectric modules with high cooling fluxes, Nat. Commun. 7 (2016) 1–7. https://doi.org/10.1038/ncomms10302.

[8] I. Chowdhury, R. Prasher, K. Lofgreen, G. Chrysler, S. Narasimhan, R. Mahajan, D. Koester, R. Alley, R. Venkatasubramanian, On-chip cooling by superlattice-based thin-film thermoelectrics, Nat. Nanotechnol. 4 (2009) 235–238. https://doi.org/10.1038/nnano.2008.417.

[9] S.B. Riffat, G. Qiu, Comparative investigation of thermoelectric air-conditioners versus vapour compression and absorption air-conditioners, Appl. Therm. Eng. 24 (2004) 1979–

1993. https://doi.org/10.1016/j.applthermaleng.2004.02.010.

[10] Z. Liu, L. Zhang, G. Gong, H. Li, G. Tang, Review of solar thermoelectric cooling technologies for use in zero energy buildings, Energy Build. 102 (2015) 207–216. https://doi.org/10.1016/j.enbuild.2015.05.029.

[11] R.A. Kishore, A. Nozariasbmarz, B. Poudel, M. Sanghadasa, S. Priya, Ultra-high performance wearable thermoelectric coolers with less materials, Nat. Commun. 10 (2019) 1765. https://doi.org/10.1038/s41467-019-09707-8.

[12] T.E. Jones, W.W. Fuller, T.J. Wieting, F. Levy, Thermoelectric power of $HfTe_5$ and $ZrTe_5$, Solid State Commun. 42 (1982) 793–798. https://doi.org/10.1016/0038-1098(82)90008-4.

[13] R.T. Littleton, T.M. Tritt, J.W. Kolis, D.R. Ketchum, Transition-metal pentatellurides as potential low-temperature thermoelectric refrigeration materials, Phys. Rev. B. 60 (1999) 13453. https://doi.org/10.1103/PhysRevB.60.13453.

[14] T.M. Tritt, R.T. Littleton, Thermoelectric properties of the transition metal pentatellurides: potential low-temperature thermoelectric materials, Semicond. Semimetals. 70 (2001) 179–206.

[15] J. Guo, Y. Huang, X. Wu, Q. Wang, X. Zhou, X. Xu, B. Li, Thickness-Dependent In-Plane Thermal Conductivity and Enhanced Thermoelectric Performance in p-Type $ZrTe_5$ Nanoribbons, Phys. Status Solidi - Rapid Res. Lett. 13 (2019) 1800529. https://doi.org/10.1002/pssr.201800529.

[16] Y.-Y. Zhang, C. Di, Y.-Y. Lv, S.-T. Dong, J. Zhou, S.-H. Yao, Y.B. Chen, M.-H. Lu, Y.-F. Chen, One-Order Decrease of Thermal Conductivity in Nanostructured $ZrTe_5$ and $HfTe_5$ Crystals, Cryst. Growth Des. 20 (2020) 680–687.

https://doi.org/10.1021/acs.cgd.9b01108.

[17] H. Weng, X. Dai, Z. Fang, Transition-Metal Pentatelluride $ZrTe_5$ and $HfTe_5$, Phys. Rev. X. 4 (2014) 011002. https://doi.org/10.1103/PhysRevX.4.011002.

[18] R. Wu, J.-Z. Ma, S.-M. Nie, L.-X. Zhao, X. Huang, J.-X. Yin, B.-B. Fu, P. Richard, G.-F. Chen, Z. Fang, X. Dai, H.-M. Weng, T. Qian, H. Ding, S.H. Pan, Evidence for Topological Edge States in a Large Energy Gap near the Step Edges on the Surface of $ZrTe_5$, Phys. Rev. X. 6 (2016) 021017. https://doi.org/10.1103/PhysRevX.6.021017.

[19] X.-B. Li, W.-K. Huang, Y.-Y. Lv, K.-W. Zhang, C.-L. Yang, B.-B. Zhang, Y.B. Chen, S.-H. Yao, J. Zhou, M.-H. Lu, L. Sheng, S.-C. Li, J.-F. Jia, Q.-K. Xue, Y.-F. Chen, D.-Y. Xing, Experimental Observation of Topological Edge States at the Surface Step Edge of the Topological Insulator $ZrTe_5$, Phys. Rev. Lett. 116 (2016) 176803. https://doi.org/10.1103/PhysRevLett.116.176803.

[20] G. Manzoni, L. Gragnaniello, G. Autès, T. Kuhn, A. Sterzi, F. Cilento, M. Zacchigna, V. Enenkel, I. Vobornik, L. Barba, F. Bisti, P. Bugnon, A. Magrez, V.N. Strocov, H. Berger, O. V. Yazyev, M. Fonin, F. Parmigiani, A. Crepaldi, Evidence for a Strong Topological Insulator Phase in $ZrTe_5$, Phys. Rev. Lett. 117 (2016) 237601. https://doi.org/10.1103/PhysRevLett.117.237601.

[21] A. Pariari, P. Mandal, Coexistence of topological Dirac fermions on the surface and three-dimensional Dirac cone state in the bulk of $ZrTe_5$ single crystal, Sci. Rep. 7 (2017) 40327. https://doi.org/10.1038/srep40327.

[22] G. Manzoni, L. Gragnaniello, G. Autès, T. Kuhn, A. Sterzi, F. Cilento, M. Zacchigna, V. Enenkel, I. Vobornik, L. Barba, F. Bisti, P. Bugnon, A. Magrez, V.N. Strocov, H. Berger, O. V. Yazyev, M. Fonin, F. Parmigiani, A. Crepaldi, Evidence for a Strong Topological

Insulator Phase in $ZrTe_5$, Phys. Rev. Lett. 117 (2016) 237601. https://doi.org/10.1103/PhysRevLett.117.237601.

[23] R.Y. Chen, Z.G. Chen, X.-Y. Song, J.A. Schneeloch, G.D. Gu, F. Wang, N.L. Wang, Magnetoinfrared Spectroscopy of Landau Levels and Zeeman Splitting of Three-Dimensional Massless Dirac Fermions in $ZrTe_5$, Phys. Rev. Lett. 115 (2015) 176404. https://doi.org/10.1103/PhysRevLett.115.176404.

[24] Y. Liu, X. Yuan, C. Zhang, Z. Jin, A. Narayan, C. Luo, Z. Chen, L. Yang, J. Zou, X. Wu, S. Sanvito, Z. Xia, L. Li, Z. Wang, F. Xiu, Zeeman splitting and dynamical mass generation in Dirac semimetal $ZrTe_5$, Nat. Commun. 7 (2016) 12516. https://doi.org/10.1038/ncomms12516.

[25] L. Zhou, A. Ramiere, P.B. Chen, J.Y. Tang, Y.H. Wu, X. Lei, G.P. Guo, J.Q. He, Anisotropic Landau level splitting and Lifshitz transition induced magnetoresistance enhancement in ZrTe5 crystals, New J. Phys. 21 (2019) 093009.

[26] Q. Li, D.E. Kharzeev, C. Zhang, Y. Huang, I. Pletikosić, A. V. Fedorov, R.D. Zhong, J.A. Schneeloch, G.D. Gu, T. Valla, Chiral magnetic effect in $ZrTe_5$, Nat. Phys. 12 (2016) 550–554. https://doi.org/10.1038/nphys3648.

[27] T. Liang, J. Lin, Q. Gibson, S. Kushwaha, M. Liu, W. Wang, H. Xiong, J.A. Sobota, M. Hashimoto, P.S. Kirchmann, Z.-X. Shen, R.J. Cava, N.P. Ong, Anomalous Hall effect in $ZrTe_5$, Nat. Phys. 14 (2018) 451–455. https://doi.org/10.1038/s41567-018-0078-z.

[28] F. Tang, Y. Ren, P. Wang, R. Zhong, J. Schneeloch, S.A. Yang, K. Yang, P.A. Lee, G. Gu, Z. Qiao, L. Zhang, Three-dimensional quantum Hall effect and metal–insulator transition in $ZrTe_5$, Nature. 569 (2019) 537–541. https://doi.org/10.1038/s41586-019-1180-9.

[29] N.D. Lowhorn, T.M. Tritt, E.E. Abbott, J.W. Kolis, Enhancement of the power factor of the transition metal pentatelluride $HfTe_5$ by rare-earth doping, Appl. Phys. Lett. 88 (2006) 022101. https://doi.org/10.1063/1.2162703.

[30] H. Wang, H. Liu, Y. Li, Y. Liu, J. Wang, J. Liu, J.-Y. Dai, Y. Wang, L. Li, J. Yan, D. Mandrus, X.C. Xie, J. Wang, Discovery of log-periodic oscillations in ultraquantum topological materials, Sci. Adv. 4 (2018) eaau5096. https://doi.org/10.1126/sciadv.aau5096.

[31] M.K. Hooda, C.S. Yadav, Enhanced thermopower and low thermal conductivity in p-type polycrystalline $ZrTe_5$, Appl. Phys. Lett. 111 (2017) 053902. https://doi.org/10.1063/1.4997460.

[32] S.A. Miller, I. Witting, U. Aydemir, L. Peng, A.J.E. Rettie, P. Gorai, D.Y. Chung, M.G. Kanatzidis, M. Grayson, V. Stevanović, E.S. Toberer, G.J. Snyder, Polycrystalline $ZrTe_5$ Parametrized as a Narrow-Band-Gap Semiconductor for Thermoelectric Performance, Phys. Rev. Appl. 9 (2018) 014025. https://doi.org/10.1103/PhysRevApplied.9.014025.

[33] S.-S. Chen, X. Li, Y.-Y. Lv, L. Cao, D. Lin, S.-H. Yao, J. Zhou, Y.B. Chen, Electrical, magneto-transport and significant thermoelectric properties of Te-rich $ZrTe_{5+\delta}$ polycrystals, J. Alloys Compd. 764 (2018) 540–544. https://doi.org/10.1016/j.jallcom.2018.06.115.

[34] B. Liu, J. Hu, J. Zhou, R. Yang, Thermoelectric Transport in Nanocomposites, Materials (Basel). 10 (2017) 418. https://doi.org/10.3390/ma10040418.

[35] W. Liu, J. Hu, S. Zhang, M. Deng, C.-G. Han, Y. Liu, New trends, strategies and opportunities in thermoelectric materials: A perspective, Mater. Today Phys. 1 (2017) 50–60. https://doi.org/10.1016/j.mtphys.2017.06.001.

[36] Y.-Y. Lv, F. Zhang, B.-B. Zhang, B. Pang, S.-H. Yao, Y.B. Chen, L. Ye, J. Zhou, S.-T. Zhang, Y.-F. Chen, Microstructure, growth mechanism and anisotropic resistivity of quasi-one-dimensional $ZrTe_5$ crystal, J. Cryst. Growth. 457 (2017) 250–254. https://doi.org/10.1016/j.jcrysgro.2016.04.042.

[37] S. Li, C. Xin, X. Liu, Y. Feng, Y. Liu, J. Zheng, F. Liu, Q. Huang, Y. Qiu, J. He, J. Luo, F. Pan, 2D hetero-nanosheets to enable ultralow thermal conductivity by all scale phonon scattering for highly thermoelectric performance, Nano Energy. 30 (2016) 780–789. https://doi.org/10.1016/j.nanoen.2016.09.018.

[38] H. Fjellvåg, A. Kjekshus, Structural properties of $ZrTe_5$ and $HfTe_5$ as seen by powder diffraction, Solid State Commun. 60 (1986) 91–93. https://doi.org/10.1016/0038-1098(86)90536-3.

[39] P. Shahi, D.J. Singh, J.P. Sun, L.X. Zhao, G.F. Chen, Y.Y. Lv, J. Li, J.-Q. Yan, D.G. Mandrus, J.-G. Cheng, Bipolar Conduction as the Possible Origin of the Electronic Transition in Pentatellurides: Metallic vs Semiconducting Behavior, Phys. Rev. X. 8 (2018) 021055. https://doi.org/10.1103/PhysRevX.8.021055.

[40] N.C. Halder, C.N.J. Wagner, Separation of particle size and lattice strain in integral breadth measurements, Acta Crystallogr. 20 (1966) 312–313. https://doi.org/10.1107/s0365110x66000628.

[41] A.Gholizadeh, X-Ray Peak Broadening Analysis in LaMnO3+δ Nano-Particles with RhombohedralCrystal Structure, J. Adv. Mater. Process. 3 (2015) 71–83.

[42] P.M. Kibasomba, S. Dhlamini, M. Maaza, C.P. Liu, M.M. Rashad, D.A. Rayan, B.W. Mwakikunga, Strain and grain size of TiO 2 nanoparticles from TEM, Raman spectroscopy and XRD: The revisiting of the Williamson-Hall plot method, Results Phys.

9 (2018) 628–635. https://doi.org/10.1016/j.rinp.2018.03.008.

[43] R. De Boer, E.H.P. Cordfunke, Phase diagram of the zirconium-tellurium system, J. Alloys Compd. 259 (1997) 115–121. https://doi.org/10.1016/S0925-8388(97)00054-6.

[44] G. Tan, L.D. Zhao, M.G. Kanatzidis, Rationally Designing High-Performance Bulk Thermoelectric Materials, Chem. Rev. 116 (2016) 12123–12149. https://doi.org/10.1021/acs.chemrev.6b00255.

[45] G.J. Snyder, E.S. Toberer, Complex thermoelectric materials, in: Nat. Mater., 2008: pp. 105–114. https://doi.org/10.1142/9789814317665_0016.

[46] W. Kim, Strategies for engineering phonon transport in thermoelectrics, J. Mater. Chem. C. 3 (2015) 10336–10347. https://doi.org/10.1039/c5tc01670c.

[47] K.W. Boer, U.W. Pohl, Semiconductor Physics, in: Springer, 2018: p. part VI. https://doi.org/10.1007/978-3-319-69150-3.

[48] M. Ohta, P. Jood, M. Murata, C.H. Lee, A. Yamamoto, H. Obara, An Integrated Approach to Thermoelectrics: Combining Phonon Dynamics, Nanoengineering, Novel Materials Development, Module Fabrication, and Metrology, Adv. Energy Mater. 1801304 (2018) 1–29. https://doi.org/10.1002/aenm.201801304.

[49] W. Gao, Z. Wang, J. Huang, Z. Liu, Extraordinary thermoelectric performance realized in hierarchically structured AgSbSe2 with ultralow thermal conductivity, ACS Appl. Mater. Interfaces. 10 (2018) 18685–18692. https://doi.org/10.1021/acsami.8b03243.

[50] J. Zhu, T. Feng, S. Mills, P. Wang, X. Wu, L. Zhang, S.T. Pantelides, X. Du, X. Wang, Record-Low and Anisotropic Thermal Conductivity of a Quasi-One-Dimensional Bulk $ZrTe_5$ Single Crystal, ACS Appl. Mater. Interfaces. 10 (2018) 40740–40747. https://doi.org/10.1021/acsami.8b12504.

[51] R. Shaviv, E.F. Westrum, H. Fjellvåg, A. Kjekshus, $ZrTe_5$ and $HfTe_5$: The heat capacity and derived thermophysical properties from 6 to 350 K, J. Solid State Chem. 81 (1989) 103–111. https://doi.org/10.1016/0022-4596(89)90207-7.